

Bypass transition in a boundary layer flow induced by plasma actuators

Dandan Xiao¹, Huw Borradaile¹, Kwing-So Choi¹, Lihao Feng²,
Jinjun Wang² and Xuerui Mao¹†

¹ Faculty of Engineering, University of Nottingham, Nottingham, NG7 2RD, UK

² Institute of Fluid Mechanics, Beihang University, Beijing, 100191, PR China

(Received 14 September 2021)

Bypass transition in flow over a flat plate triggered by a pair of Dielectric-barrier-discharge (DBD) plasma actuators mounted on the plate surface and aligned in the streamwise direction is investigated. A 4-species plasma-fluid model is used to model the electrohydrodynamic (EHD) force generated by the plasma actuation. A pair of counter-rotating streamwise vortices is created downstream of the actuators, leading to the formation of a high-speed streak in the centre and two low-speed streaks on each side. As the length of actuators increases, more momentum is added to the boundary layer and eventually a turbulent wedge is generated at an almost fixed location. With large spanwise distance between the actuators (wide layout), direct numerical simulations (DNS) indicate that the low-speed streaks on both sides lose secondary stability via an inclined varicose-like mode simultaneously, leaving a symmetric perturbation pattern with respect to the centre of the actuators. Further downstream, the perturbations are tilted by the mean shear of the high- and low-speed streaks and consequently a ‘W’ shape pattern is observed. When the pair of plasma actuators is placed closer (narrow layout) in the spanwise direction, the mean shear in the centre becomes stronger and secondary instability first occurs on the high-speed streak with an asymmetric pattern. Inclined varicose-like and sinuous-like instabilities coexist in the following breakdown of the negative streaks on the side and the perturbations remain asymmetric with respect to the centre. Here the tilting of disturbances is dominated by the mean shear in the centre and the perturbations display a ‘V’ shape. Linear analysis techniques including biglobal stability and transient growth are performed to further examine the fluid physics and the aforementioned phenomena at narrow and wide layouts, such as the secondary instabilities, ‘V’ and ‘W’ shapes, the symmetric and asymmetric breakdown, are all observed.

1. Introduction

Bypass transition has been well observed and studied in turbo-machinery owing to its significant impacts on the performance of the machine. The term bypass transition is used for all transition processes that bypass the classic transition route via the exponential growth of Tollmien-Schlichting (TS) waves. There have been enormous studies on the onset of bypass transition, mostly induced by free stream turbulence (Matsubara & Alfredsson 2001; Fransson *et al.* 2005; Jacobs & Durbin 2001; Brandt & Henningson 2004, just to name a few). Bypass transition can also develop in the presence of surface elements, which has been widely investigated experimentally (Gaster *et al.* 1994; White 2002; Downs *et al.* 2008) and numerically (Tullio *et al.* 2013; Goldstein *et al.* 2017; Bucci *et al.* 2018). In this work, we study numerically the flow development downstream of a

† maoxuerui@sina.com

pair of streamwise-aligned plasma actuators analogous to roughness elements and focus on the bypass transition when the actuators are sufficiently long.

1.1. Bypass transition

The early stage of bypass transition involves the formation of streaks due to the lift-up of the mean momentum (Taylor 1939; Landahl 1975). The low-momentum (high-momentum) fluid is displaced upwards (downwards) by a small positive (negative) wall-normal velocity disturbance, leading to high- and low- speed streaks. When the boundary layer is subject to free stream turbulence, streaks are formed as a result of the low-frequency disturbances entering the boundary layer via shear sheltering (Hunt & Durbin 1999) and then tilting the base shear via the lift-up (Landahl 1980). Using linear optimal disturbance analysis, it has been found that the optimal inflow condition leading to the maximum transient energy growth downstream is a pair of steady streamwise-aligned vortices, resulting in a pair of streamwise velocity streaks (Butler & Farrell 1992; Andersson *et al.* 1999; Monokrousos *et al.* 2010).

After generation, the streaks are further amplified as they are convected downstream. It was reported that the amplitude of the streaks increases as the square root of the distance from the leading edge (Kendall 1985). The streaks interact with the streamwise vorticity and the high- (low-) speed streaks are lifted towards (away from) the wall via a nonlinear lift-up mechanism, leaving an inflection point in the mean shear profile that is prone to secondary instabilities (Mao *et al.* 2017). Swearingen & Blackwelder (1987) first identified two forms of secondary instability leading to the breakdown of streaks in Görtler flow: a sinuous type and a varicose type. The sinuous mode is associated with the spanwise inflectional velocity profile and features an asymmetric pattern with respect to the unstable streak, whereas the varicose one is related to the wall-normal inflection point and presents a symmetric pattern. The sinuous instability usually occurs around the low-speed streak that is lifted upwards and varicose instability is found in the overlapping region between the high- and low-speed streaks (Vaughan & Zaki 2011; Hack & Zaki 2014). Andersson *et al.* (2001) performed inviscid instability analysis on optimal streaks and found the critical streak amplitudes are 26% and 37% for the sinuous and varicose instabilities, respectively. More recently, Puckert & Rist (2019) observed in experiments that the sinuous and varicose modes coexist in the wake of a roughness element and the two modes are coupled with frequency lock-in.

The development of streak instabilities results in either turbulent spots or turbulent wedges which eventually lead to transition to turbulence. Turbulent spot is commonly found in boundary layer flow subject to free stream turbulence. Turbulent wedge, on the other hand, is a turbulent region bounded by a transitional region that develops in the spanwise direction as it propagates downstream (Schubauer & Klebanoff 1955). The turbulent wedge is generally found in roughness induced bypass transition and is reported to spread laterally at a half-angle of $\sim 6^\circ$ (Zhong *et al.* 2003; Goldstein *et al.* 2017).

1.2. Plasma actuators

Dielectric-barrier-discharge (DBD) plasma actuators are electric devices which introduce the fluid flow by coupling the momentum. When the actuation is applied with a large AC voltage, the fluid near the surface is ionised and the charged particles are accelerated by the electric field. In this way the plasma actuators introduce momentum via collision between the charged particles and the ambient fluid (Boeuf *et al.* 2007), which can be modelled as an electrohydrodynamic (EHD) body force that produces a jet flow up to 10m/s (Moreau 2007). When the plasma actuators are placed along the streamwise

direction in a boundary layer, a body force in the spanwise direction is generated that results in a spanwise-directed wall jet. Jukes & Choi (2013) found that the interaction between this wall jet and the oncoming boundary layer leads to the formation of a coherent streamwise vortex. More recently, Choi & Kim (2018) performed experiments on ring-type plasma actuators, which act as virtual roughness elements, and found that the body force leads to a wall-normal jet. In flow control, the body force induced by the DBD plasma actuators have been used for the delay of classic (Grundmann & Tropea 2008; Riherd & Roy 2013; Duchmann *et al.* 2014) and bypass transition (Lavoie *et al.* 2010; Riherd & Roy 2014; Bade *et al.* 2016), the suppression of flow separation (Schatzman & Thomas 2010; Walker & Segawa 2012; Giorgi *et al.* 2017), drag reduction (Wilkinson 2003; Choi *et al.* 2011) and lift enhancement (Little *et al.* 2010; Greenbelt *et al.* 2012; Feng *et al.* 2012).

The numerical simulation of DBD plasma actuators has been extensively studied as it allows detailed examination of the induced flow. In these works the model of DBD plasma actuators can be divided into two groups: simplified phenomenological models and first-principle based models (Mahfoze & Laizet 2017). Simplified models assume that the response of fluid flow and the formation of plasma are decoupled due to large differences in the characteristic velocities associated with each process (Mertz & Corke 2011). Popular simplified phenomenological models include Shyy (Shyy *et al.* 2002) model and the Suzen & Huang model (Suzen *et al.* 2005). On the other hand, first-principle based models aim at modelling the physical mechanisms of the plasma actuator and thus providing better accuracy (Nishida *et al.* 2014; Dufour & Rogier 2015). Consequently transport equations for both the charged and neutral species as well as a Poisson equation for the electric field are solved to obtain the EHD body force, as will be adopted in the present work.

The paper is organised as follows. In § 2, the numerical method including the plasma model is introduced. In § 3 the problem description and computational set-up are presented. The results are reported in § 4. First, the plasma body force in the boundary layer is displayed in § 4.1, followed by a presentation of the wake flow downstream of the actuators in § 4.2. Then parametric study is performed and analysed in § 4.3 and finally the secondary instability and Orr mechanism observed during the breakdown of plasma induced bypass transition is investigated in § 4.4 and 4.5, respectively. In § 5, biglobal stability and transient growth analysis are performed to further examine the mechanism of transition revealed in DNS. In § 6, the main observations are summarised.

2. Numerical scheme

Plasma actuation in incompressible boundary layer flow over a flat plate is considered in this work. The flow is governed by the Navier-Stokes (NS) equations:

$$\partial_t \mathbf{u} + \mathbf{u} \cdot \nabla \mathbf{u} + \nabla p - Re^{-1} \nabla^2 \mathbf{u} + \mathbf{F} = 0, \quad \nabla \cdot \mathbf{u} = 0, \quad (2.1)$$

where $\mathbf{u} = (u, v, w)^T$, p and \mathbf{F} denote the non-dimensional velocity, pressure and external force induced by the plasma actuation, respectively. u , v and w are the streamwise, wall-normal and spanwise velocity component, respectively. Re is the Reynolds number defined as $Re = U_\infty R / \nu$, where ν is the kinematic viscosity, U_∞ is the free stream velocity and R is the half thickness of the flat plate, which are used as the reference velocity and length, respectively. The velocity vector can be decomposed as,

$$\mathbf{u} = \bar{\mathbf{U}} + \mathbf{u}'', \quad (2.2)$$

where \mathbf{u}'' is the velocity fluctuation and $\bar{\mathbf{U}}$ is the mean flow that can be further decomposed as:

$$\bar{\mathbf{U}} = \mathbf{U} + \mathbf{u}', \quad (2.3)$$

where \mathbf{U} is the two-dimensional base flow when the plasma is not activated, satisfying equation (2.1) when $\mathbf{F} = 0$, and \mathbf{u}' represents the mean disturbance induced by the plasma force. Just for clarity, in the rest of this paper $\mathbf{u}' + \mathbf{u}''$ is referred to as total perturbation or disturbance and \mathbf{u}'' is referred to as perturbation or disturbance.

\mathbf{F} in equation (2.1) is a force representing the cycle-averaged EHD force \mathbf{F}_{EHD} ,

$$\mathbf{F}_{EHD} = \sum_i n_i q_i \mathbf{E}, \quad (2.4)$$

where n_i and q_i are the density and charge of the i -th species composing the plasma, respectively, and \mathbf{E} denotes the electric field. The integration of \mathbf{F}_{EHD} results in a steady force $\mathbf{F} = 1/\tau \int_0^\tau \mathbf{F}_{EHD} dt$ and the time-variation of \mathbf{F}_{EHD} is not considered in equation (2.1). This simplification is due to the large gap between the time-scales of the plasma dynamics and the fluid dynamics. A 4-species plasma-fluid model (Dufour & Rogier 2015), which solves the fluid equations for four species is used to model the discharge mechanics of the DBD plasma actuators. To simulate the dynamics of each species, the conservation equations for their densities are considered,

$$\partial_t n_i + \nabla \cdot (n_i \mathbf{v}_i) = S_i, \quad (2.5)$$

where \mathbf{v}_i are the velocity of the i -th species. The last term S_i represents the source term accounting for the creation of the charged species due to chemical reactions. The chemical reactions, describing the interaction between the electrons and the positive, negative and neutral particles, include ionisation, attachment, electron-ion and ion-ion recombination. The rate coefficients for these reactions are obtained using BOLSIG+ (Hagelaar & Pitchford 2005) and the LXCat databases (Phelps 2012; Pitchford & Boeuf 2012). Neglecting the magnetic and inertial terms of the momentum equation, the velocity of the species can be obtained as follows,

$$\mathbf{v}_i = \mu_i \mathbf{E} + D_i \frac{\nabla n_i}{n_i}, \quad (2.6)$$

where μ_i and D_i are the mobility and diffusion coefficients of the corresponding species, respectively.

The electric field \mathbf{E} is obtained by solving a Poisson equation for the electric potential ϕ :

$$\nabla \cdot (\epsilon \nabla \phi) = \sum_i n_i q_i \quad \text{and} \quad \mathbf{E} = -\nabla \phi, \quad (2.7)$$

where ϵ is the local material permittivity.

3. Problem description and computational domain

A schematic diagram of the geometry of a flat plate with a slender leading edge is shown in figure 1(a). The computational domain spans from $x = -20$ to $x = 200$ in the streamwise direction, and from $y = -40$ to $y = 40$ in the wall-normal direction. The leading edge is located at $x = 0$ with an elliptic shape and aspect ratio $AR = 20$.

As aforementioned, the steady two-dimensional base flow \mathbf{U} is obtained by integrating the full nonlinear Navier-Stokes equations (2.1) with $\mathbf{F} = 0$ until a steady solution is reached. Figure 1(b) shows the base flow profile over the upper part of the flat plate at

$Re = 800$, which will be used in all the rest of this work. Downstream of the leading edge, the flow develops into a zero-pressure-gradient boundary layer and the boundary layer thickness is approximately $\delta = 1.8$ at the end of the computational domain. The shape factor is computed at various locations downstream of the leading edge and is all around 2.52. Validation of the simulation can be found in Wang *et al.* (2019).

The numerical code used here has been extensively validated in previous works for various flow problems, such as backward-facing step (Barkley *et al.* 2008; Mao 2015), flat plate with leading edge (Wang *et al.* 2019; Huang *et al.* 2021), etc. The governing equations are discretised in the $x - y$ plane using the spectral element method into 2505 elements, most of which are clustered around the upper side of the plate where the plasma actuation and bypass transition will be investigated. Each element is further decomposed into a $(\mathcal{P} + 1) \times (\mathcal{P} + 1)$ grid, where \mathcal{P} is the polynomial order that defines the resolution. In this work, $\mathcal{P} = 8$ is adopted, i.e. the spatial order of discretization is 8. In the spanwise direction, the flow variables are decomposed as,

$$\mathbf{u}(x, y, z) = \sum_{n=0}^{n_z} \mathbf{u}_\beta(x, y) e^{i\beta z}, \quad (3.1)$$

where a total of $n_z = 192$ Fourier modes over the spanwise width of the domain 12 are computed. Moreover, the temporal order of discretization is set to 2. Detailed description of the boundary conditions can be found in Wang *et al.* (2019) and Huang *et al.* (2021).

The two-dimensional EHD force distribution of a single plasma actuator is computed separately in a dimensional setting by the 4-species plasma-fluid model described in § 2. The thicknesses of the upper/lower electrodes and the dielectric sheet are $50 \mu m$ and $150 \mu m$, respectively. The distance between the upper and lower electrode edge is $L_e = 1 mm$, as indicated in figure 1(a). The AC voltage applied to the plasma actuators is sinusoidal with an amplitude of $2 kV$ and three frequencies, $f = 20 kHz$, $40 kHz$ and $60 kHz$ are considered. The computational domain contains 58795 elements of which 46136 are in the fluid domain. The 2D force distribution is non-dimensionalised using density ($1.225 kg/m^3$) and viscosity ($1.81 \times 10^{-5} kg/(m \cdot s)$) of air before applying to the three-dimensional boundary layer. This model and its numerical discretization have been validated in various configurations for atmospheric pressure plasma discharges (Kourtzanidis *et al.* 2020a,b).

The arrangement of the DBD plasma actuators on the plate is shown in figure 1(a). Plasma actuators with different lengths of the upper electrode are tested and it is found that the force topology remains the same as long as L_e is fixed over the parameters considered in this work. The actuators generate a jet-like velocity in the spanwise direction. This leads to a wall-ward velocity component above the actuators because fluid is brought towards the actuator from above to replace those drawn away laterally by the EHD body force (Jukes & Choi 2013). The upstream edge of the plasma actuators is located at $x = 30$, where the Reynolds number based on boundary layer thickness at this location is $Re_\delta = 560$. Different streamwise lengths of the plasma actuator ranging from $L_x = 10$ to $L_x = 90$ are investigated. The two plasma actuators are placed with respect to the centre position of the domain $z = 6$ and the spanwise distance of the upper electrode L_z ranging from 0.1 to 1.5 are considered.

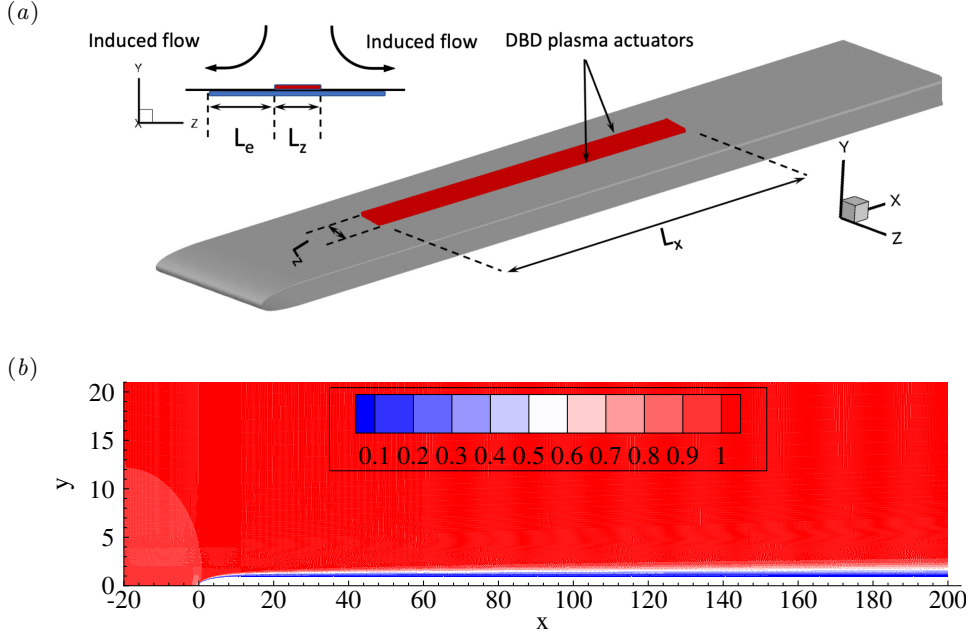


FIGURE 1. (a) Schematics of plasma actuators on the flat plate; (b) contour of the streamwise velocity component of the base flow around the upper part of the flat plate at $Re = 800$, which will be used in all the following studies.

4. Plasma induced transition

4.1. Plasma induced body forcing

Figure 2 shows the distribution of the wall-normal and spanwise components of the EHD force exerted by the plasma actuators at 60 kHz denoted as F_y and F_z , respectively. The plasma actuators are arranged to produce vertical velocity towards the wall as seen in figure 1(a). In figure 1(b), the spanwise component on each side has two opposing regions, which is due to the PUSH-pull scenario of the AC cycle (Thomas *et al.* 2010). The larger force region dominates and leads to an outward jet from the centre. A separate simulation of the plasma force in quiescent air is performed in order to examine the effect of actuator. The momentum coefficient (Jukes & Choi 2012) computed at $z = 6.65$, where the spanwise velocity reaches its maximum value, is around 0.018%. Note that the minor difference in the two opposing force distributions is due to linear interpolation of the force when applied to the boundary layer flow domain. The force reaches $y = 1.08$, while the edge of the boundary layer at the upstream edge of the actuator is at about $y = 1.7$.

The effect of actuation frequency on the generated EHD force is shown in figure 3. As the frequency is increased from 20 kHz to 60 kHz , the variation in the resultant force direction is less than 8° . On the other hand, the magnitude of the spanwise component of the force increases with the frequency. This suggests that the plasma actuators are capable of inducing body force of a wide range of strength, whilst maintaining a relatively consistent force distribution and direction. In the rest of this work the frequency is set to 60 kHz unless otherwise stated. The frequency corresponds to a non-dimensionalised value of around 31.4, which is two-orders higher than the high frequency disturbance mode (0.32 – 0.64) used to trigger bypass transition in a flat plate boundary layer flow in Zaki & Durbin (2005)

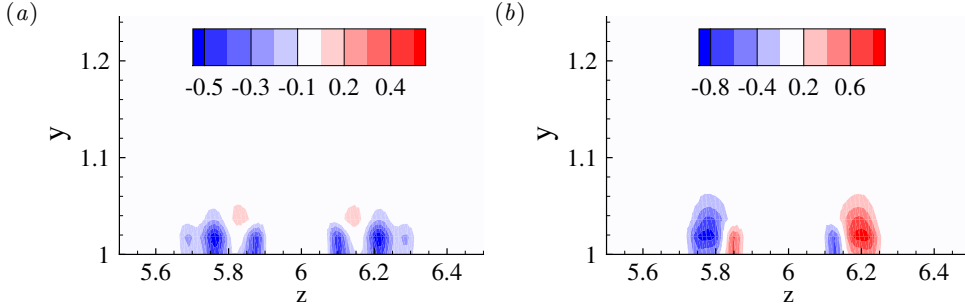


FIGURE 2. Contour of (a) wall-normal and (b) spanwise component of the EHD force distribution at 60 kHz and 2 kV, which will be used in all the following if not otherwise stated.

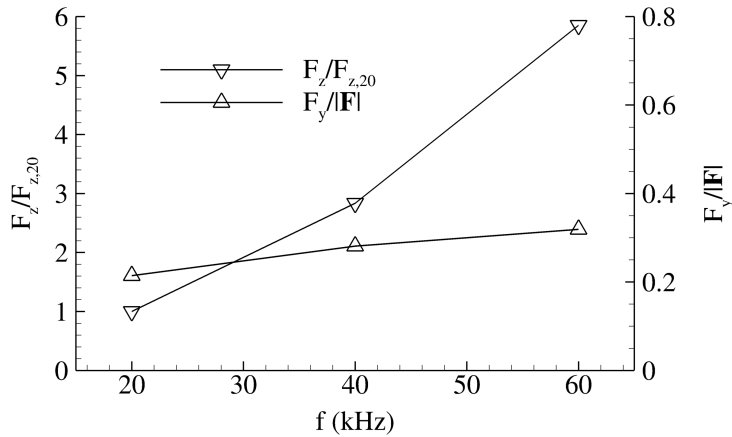


FIGURE 3. Comparison of the EHD force obtained at different frequency f . Left y-axis shows the magnitude of F_z scaled by $F_{z,20}$ (at 20 kHz); Right y-axis shows the ratio between F_y and the magnitude of the resultant force $|\mathbf{F}|$ at each frequency. All the forces are obtained by integration over the $y-z$ plane.

4.2. Wake flow of plasma actuators

Direct numerical simulations (DNS) of boundary layer flow with plasma actuations are performed. A pair of plasma actuators is placed over a flat plate in such a way that the plasma wall jets are induced away from each other, while creating an entrained flow towards the wall between the two actuators. This leads to the formation of a pair of counter-rotating vortices, as shown in figure 4. Similar phenomena were observed in experimental studies (Jukes *et al.* 2008). Jukes & Choi (2013) further suggested that the spanwise-directed wall jet interacts with the oncoming boundary layer and streamwise vortices are created as a result. In figure 4, secondary vorticity is induced below the primary vortices, which is due to the preservation of the no-slip wall boundary condition. Whalley & Choi (2013) experimentally investigated DBD plasma actuators in quiescent air and reported that the secondary vorticity wraps around the starting vortex and steers its trajectory away from the wall at an angle of 31° , which agrees well with the present observation shown in figure 4.

The wake flow downstream of the actuators with $(L_x, L_z) = (90, 0.25)$ is shown in figure 5. It is clear that the transition downstream of the plasma actuators occurs through a turbulent wedge, which is often found in turbulent flow developed in the presence of surface elements, in contrast to turbulent spots induced by free stream disturbance. The

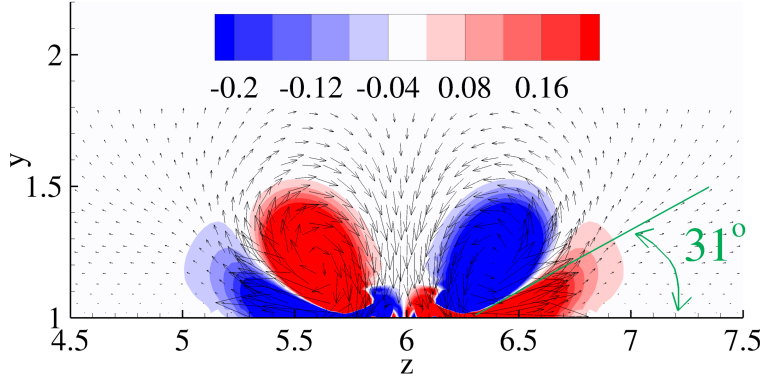


FIGURE 4. Contour of streamwise vorticity induced by the plasma actuators. The direction and length of the arrow indicate the direction and magnitude of the induced velocity.

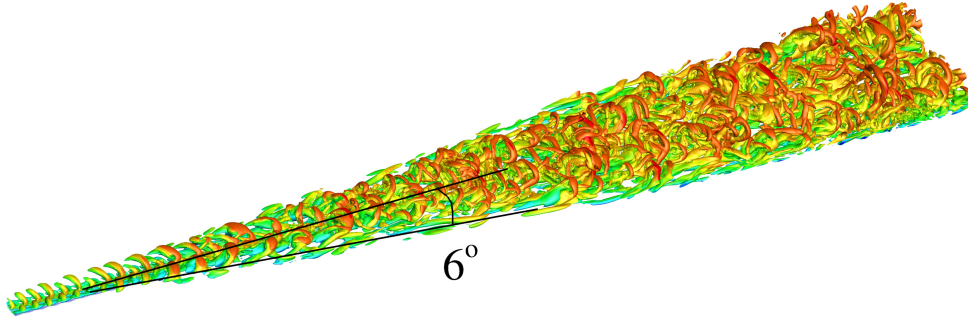


FIGURE 5. Turbulent wedge and vortical structure with $(L_x, L_z) = (90, 0.25)$, visualised with isosurface of $\lambda_2 = -0.01$ and coloured by instantaneous streamwise velocity u .

half spreading angle is approximately 6° , in agreement with those reported in literature. For example, Zhong *et al.* (2003) observed in experiment a spreading half-angle of 6.5° of turbulent wedge induced by a three-dimensional surface roughness in a laminar boundary layer flow. Goldstein *et al.* (2017) found a turbulent wedge spreading half-angle of 6° developed downstream of an asymmetric cylindrical perturbation in their numerical simulations. The spreading angles for other settings of (L_x, L_z) are all around 6° and not displayed here for brevity.

We divide the transition process induced by plasma actuations into four stages, which is demonstrated in figure 6 using the isosurfaces of streamwise vorticity. In the first stage, vortical disturbance is generated by the plasma actuators as discussed previously. Once the pair of the counter-rotating vortices is created, it is continuously supplied with streamwise vorticity from the outer layer of the spanwise jet induced by the plasma to increase the circulation (Jukes & Choi 2013). As a consequence, streaks are generated due to lift up and amplified along the streamwise direction.

As the amplitude of the disturbance grows beyond a threshold, secondary instability occurs in the second stage. In figure 6 positive/negative tilted streamwise vorticity starts to appear at $x = 70$. Similar observations were made by Saikishan *et al.* (2019) and Goldstein *et al.* (2017) along the edge of flow developed downstream of a roughness element and the patterns are named as tilted ‘pancakes’ of ω_x . From a vorticity point of view, the tilted ‘pancakes’ are a signature of the vorticity tilting process turning ω_z into ω_x and ω_y (Goldstein *et al.* 2017). Starting from $x = 82$, there is a clear expansion of the

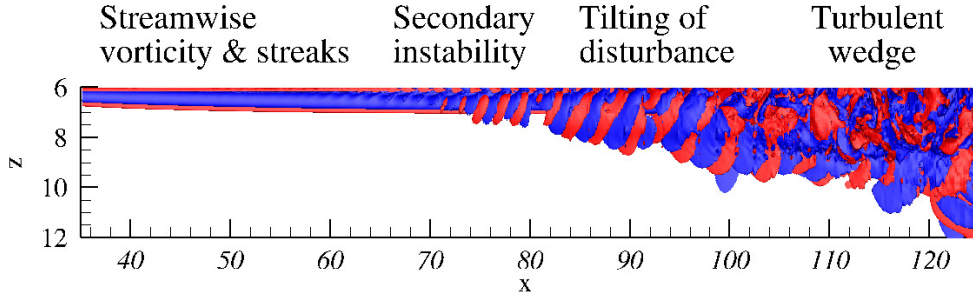


FIGURE 6. Isosurfaces of streamwise vorticity 0.1 (red) and -0.1 (blue) with $(L_x, L_z) = (90, 0.25)$. The plot shows half of the domain in the spanwise direction, which is scaled by 2.5. The four stages of the transition process are indicated at corresponding locations.

vorticity in the spanwise direction. In this stage, the shape of the disturbances is further tilted by the spanwise shear and will be elaborated later. In the final stage turbulent wedge is formed and the flow becomes turbulent. Details on the secondary instability and its further tilting by the shear will be discussed in the following sections.

4.3. Parametric study

In this section, the effects of L_x , L_z and f on the flow development are presented. Figure 7 shows the total streamwise perturbation $u' + u''$ with $L_z = 0.25$ and L_x ranging from 10 to 90. A high-speed streak can be seen in the centre with two low-speed streaks on each side. Similar results are found in the experimental work of Gouder *et al.* (2017), where a pair of plasma actuators, arranged in the same way as the current work, were used to control boundary layer streaks. In contrast, a single roughness element induces a wake consists of a central low-speed streak, surrounded by a pair of high- and low-speed ones on each side (Loiseau *et al.* 2014). The streaks in figure 7(a) grow initially, and then decay and vanish completely. For larger values of L_x , the streaks become stronger and decay downstream of the actuators as seen in figure 7(b) and (c). In figure 7(d) and (e), the streaks are strong enough to breakdown and the flow becomes turbulent.

We further investigate the effect of L_x quantitatively by examining the streak amplitude A (Cossu & Brandt 2002; Biancofiore *et al.* 2017; Wang *et al.* 2019) defined as,

$$A = \frac{1}{2} [\max(u - U) - \min(u - U)]. \quad (4.1)$$

Figure 8 presents the streak amplitude A as a function of the streamwise location x for each case in figure 7. For $L_x = 70$ and $L_x = 90$, A in the turbulent regime is not shown as it is ill-defined and does not indicate the magnitude of streaks there. It can be seen that the streak amplitude increases at almost the same rate for all the cases. For the first three steady cases, A starts to decrease immediately beyond the actuation region with a similar decay rate. These are in agreement with the experimental results in Jukes & Choi (2013), where they investigated three different lengths of plasma actuators and reported that the vortex circulation increases along the length of the plasma actuators. They also observed that the strength of the vortex starts to decrease due to the viscous effect beyond the plasma region. For the three lengths Jukes & Choi (2013) tested, the vortex strength increases with the plasma length, from which they concluded that longer and stronger vortices can be generated by increasing the length of the actuators. In figure 8, the streak amplitude initially increases almost linearly before $x = 40$ and then the growth rate gradually decreases until the peak is reached at around $x = 80$. The streaks induced

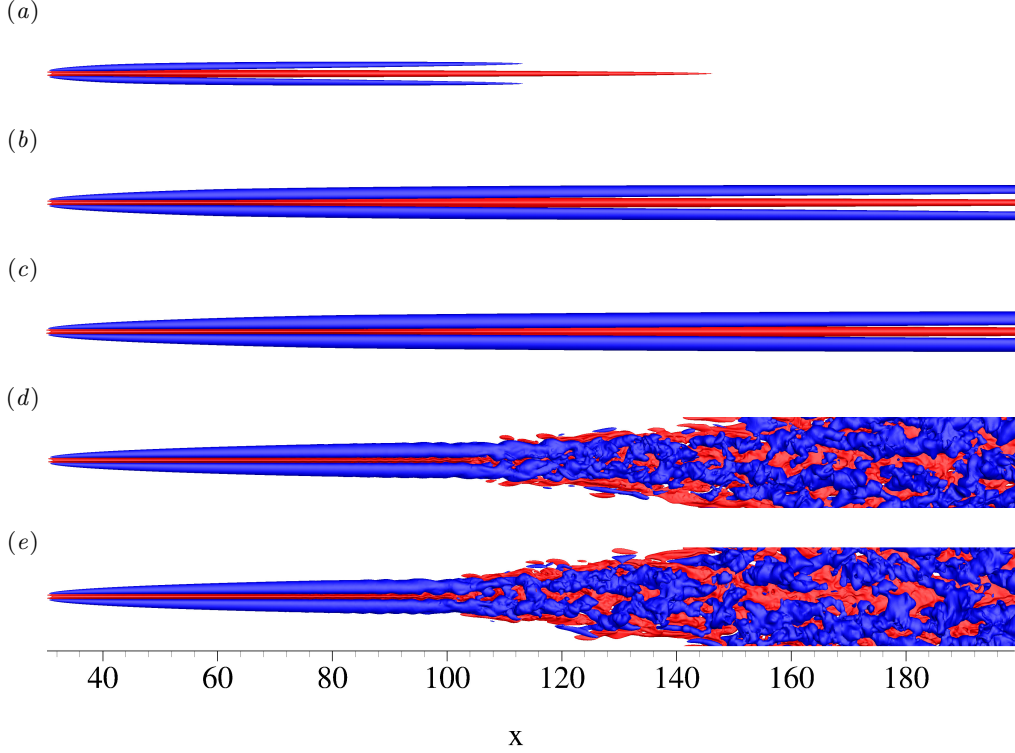


FIGURE 7. Isosurfaces of the total streamwise perturbation velocity $u' + u'' = 0.1$ (red) and $u' + u'' = -0.1$ (blue) for $L_z = 0.25$ and various L_x : (a) $L_x = 10$, (b) $L_x = 30$, (c) $L_x = 50$, (d) $L_x = 70$ and (e) $L_x = 90$.

by plasma actuators, similar to those triggered by surface roughness, are stationary and do not demonstrate randomness, in contrast to those by free stream turbulence (von Deyn *et al.* 2020). For cases where the length of plasma actuators exceeds the peak, the streak amplitude becomes large enough and the flow breaks down into turbulence. Similar bypass transition has been observed downstream of roughness elements with large enough size (von Deyn *et al.* 2020). Moreover, it can be expected that the breakdown location will remain approximately the same at even larger L_x .

Figure 9 presents the flow responses for $L_x = 90$ and L_z varying from 0.1 to 1.5. Instability starts to appear at around $x = 90$ and the streaks break down to turbulent flow for all cases except the first one. Two types of flow pattern can be observed: in figure 9(b), the positive streak undergoes asymmetric meandering motion with respect to $z = 6$ (the centre line) prior to the breakdown, while in figure 9(d) and (e), the disturbances present a symmetric pattern. This difference will be discussed later.

The effect of L_z on the streak amplitude is illustrated in figure 10. Similar as before, A in the turbulent region is ill-defined by equation (4.1) and is not shown. For $L_z = 0.1$ the streak amplitude reaches a peak value of 0.4 and becomes almost flat after $x = 60$. This is in agreement with Jukes & Choi (2013)'s prediction that some limit can be reached for very long plasma actuators because the momentum added by the plasma actuators should be balanced by the viscosity and beyond the limit, the plasma actuators can only act to maintain the vortex instead of continuously strengthening it. The streaks start to decay beyond the downstream edge of the plasma at $x = 120$. For the rest three cases with larger L_z , the streaks grow at a larger rate and reach above 0.55 at $x = 90$. The

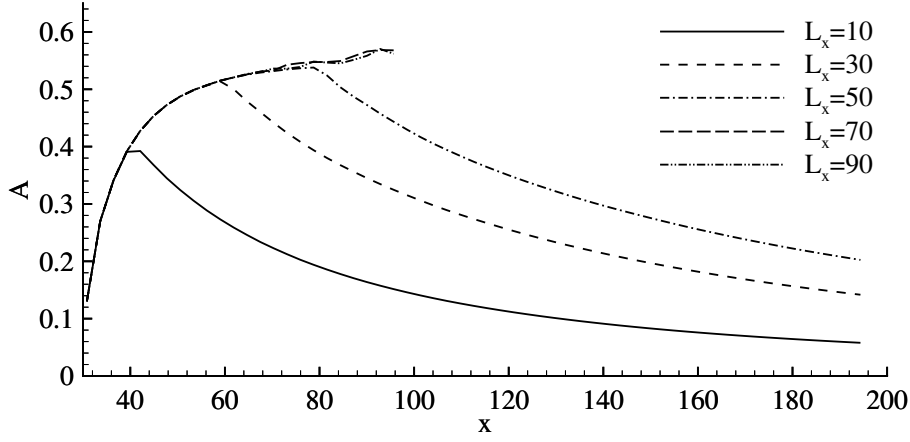


FIGURE 8. Variation of the streak amplitude A along the streamwise direction at various values of L_x and $L_z = 0.25$.

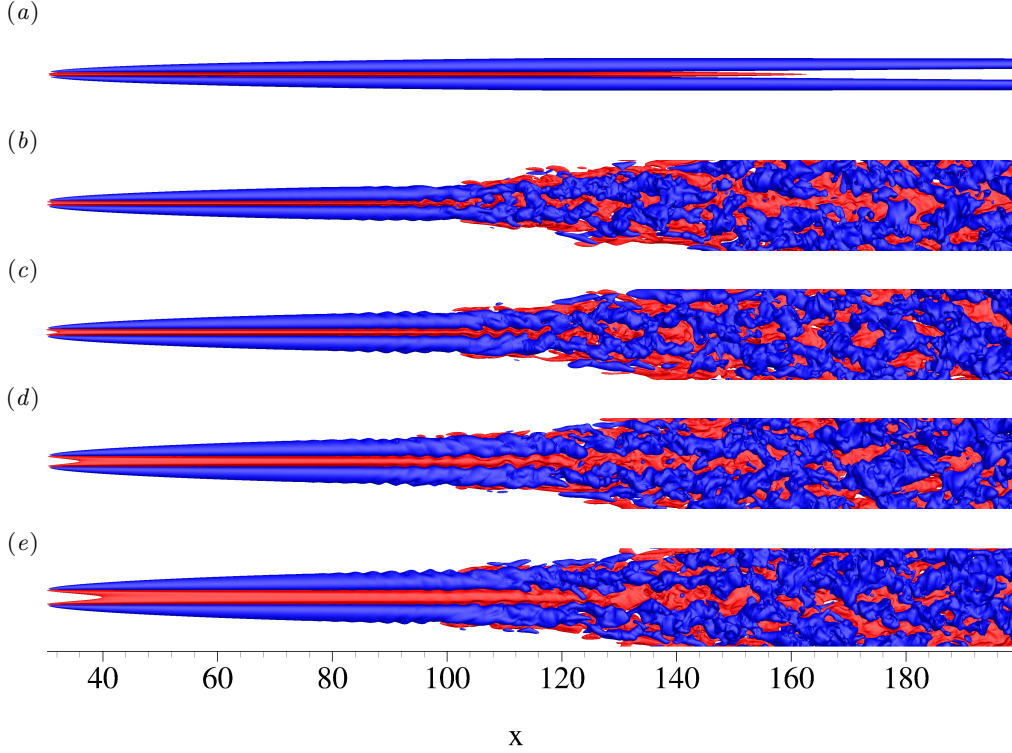


FIGURE 9. Isosurfaces of the total streamwise perturbation velocity $u' + u'' = 0.1$ (red) and $u' + u'' = -0.1$ (blue) for $L_x = 90$ and varying L_z : (a) $L_z = 0.1$, (b) $L_z = 0.25$, (c) $L_z = 0.5$, (d) $L_z = 1$ and (e) $L_z = 1.5$.

streak amplitude prior to breakdown for $L_z = 0.25$, which corresponds to the asymmetric shape in figure 9(b), is slightly smaller than the other two cases with $L_z = 0.5$ and 1, which correspond to figure 9(c) and (d).

From figure 8 and 10, it can be concluded that both L_x and L_z have significant effects on

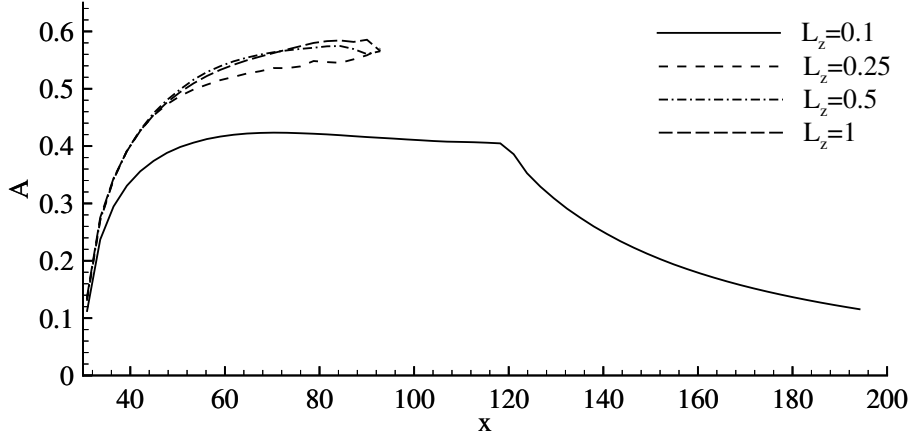


FIGURE 10. Variation of the streak amplitude A against the streamwise location x at $L_x = 90$ and various values of L_z .

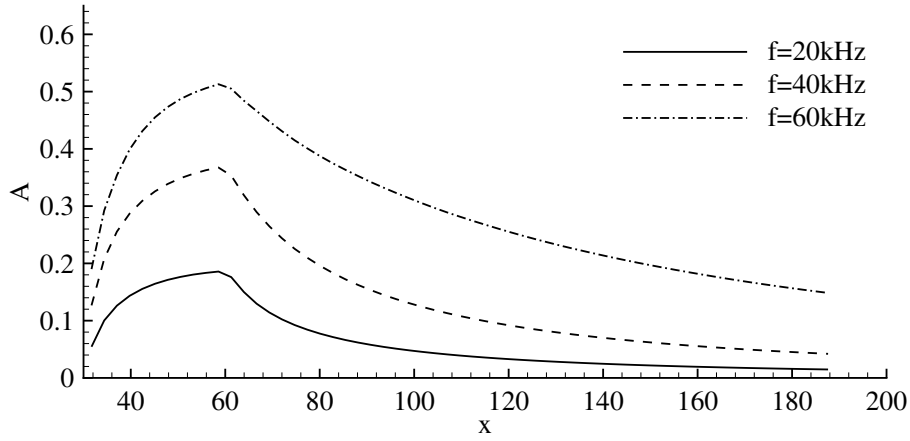


FIGURE 11. Variation of the streak amplitude A against frequency with $(L_x, L_z) = (30, 0.25)$.

the transition. Larger L_x means more energy is added to the flow by the plasma actuators and results in a larger streak amplitude that leads to turbulence. On the other hand, the maximum of the streaks grows with L_z , which is determined by the balance between the momentum added by the actuators and the viscous dissipation. Furthermore, it can be seen that the breakdown location is almost independent on L_x or L_z after passing the breakdown thresholds.

The effect of frequency of the plasma actuators on the streak amplitude is displayed in figure 11. All three frequencies generate similar behaviours, i.e. A grows with a reduced rate along x until the end of the plasma actuation region, and then starts to decrease abruptly. It can be seen that higher frequency results in a larger growth rate, which is a direct result of the increased force amplitude. The streak amplitude at $x = 60$ increases sublinearly with respect to the frequency, while in figure 3 the magnitude of force has a superlinear relationship with the frequency.

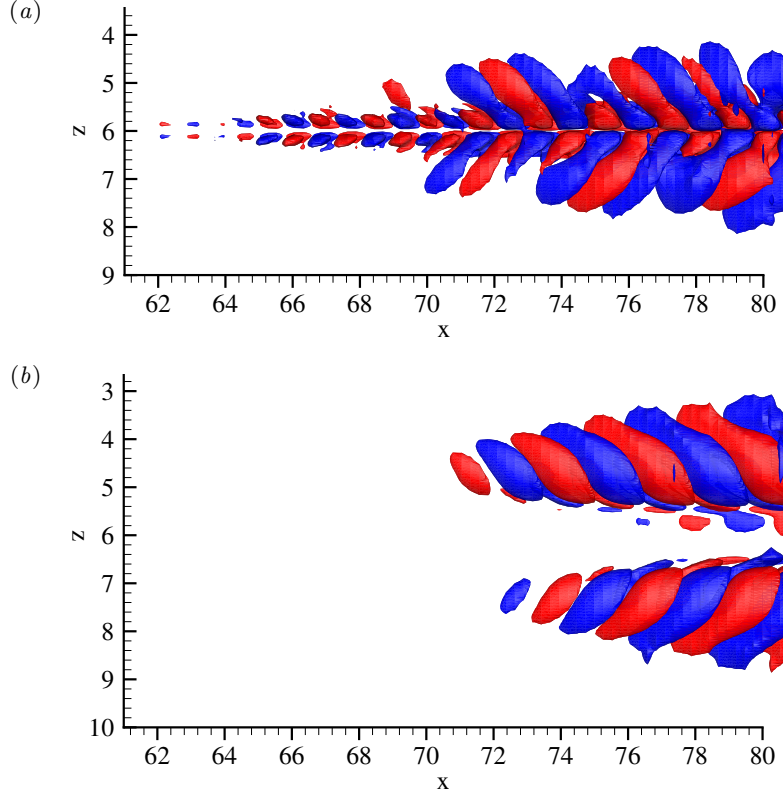


FIGURE 12. Isosurfaces of streamwise perturbation $u'' = 0.005$ (red) and $u'' = -0.005$ (blue) for (a) $(L_x, L_z) = (90, 0.25)$ and (b) $(L_x, L_z) = (90, 1)$.

4.4. Secondary instabilities of streaks

The asymmetric and symmetric patterns of the total streamwise disturbance with respect to the centre line in previous section indicate different forms of instabilities. In this section, secondary instabilities of the streaks are investigated in detail by examining two cases specifically: a narrow layout case $(L_x, L_z) = (90, 0.25)$ and a wide layout case $(L_x, L_z) = (90, 1)$, which have been shown in figure 9(b) and (d), respectively. Figure 12 presents the streamwise perturbation u'' for both the narrow and wide layouts in a zoomed-in view that only covers stage 2. In the narrow layout case, the positive streak in the centre loses stability first with u'' appearing in an asymmetric pattern from $x = 62$. The perturbations then expand to the negative streaks on the side after $x = 70$, while the asymmetry with respect to $z = 6$ is maintained. A different observation is seen in the wide layout configuration in figure 12(b): u'' first starts to appear on the negative streaks at $x = 72$. Since the instabilities are developed almost simultaneously on their own around the underlying streak, the perturbations are symmetric with respect to $z = 6$. It seems that L_z determines whether the positive streak in the centre loses stability prior to the breakdown of negative streaks, consequently affecting the appearance of u'' , i.e., asymmetric (symmetric) pattern for small (large) values of L_z . In the rest of this section, we will investigate in detail the secondary instability.

Figure 13 shows the streamwise disturbance u'' as well as the mean flow at $x = 78$ within stage 2. u'' is symmetric with respect to $z = 6$ in the narrow layout and asymmetric in the wide layout, as discussed previously. In both cases, the solid green lines connecting

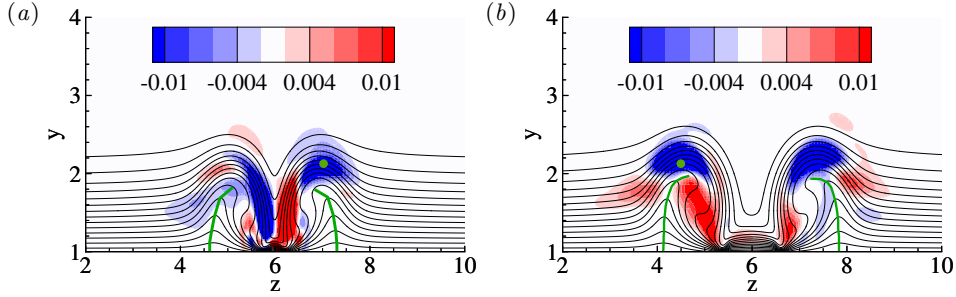


FIGURE 13. Color contour of u'' at $x = 78$ with (a) $(L_x, L_z) = (90, 0.25)$ and (b) $(L_x, L_z) = (90, 1)$. Black lines show the contour lines of the streamwise mean velocity \bar{U} from 0.1 to 1. Green lines connect the peak of \bar{U} at each contour level.

the peak of the mean flow at each contour level bend towards the centre as a result of the interaction between the positive streak at the centre and the lifted negative streaks on the side. In the narrow configuration, the disturbance on the right hand side shows an asymmetric-like pattern with respect to the inclined negative streak centre, while on the left hand side the pattern is neither symmetric nor asymmetric. In the wide layout case, u'' shows a symmetry-like pattern. The disturbances are not completely symmetric or asymmetric with respect to the unstable streak as observed in a model problem where ideal streaks are used (Brandt & Henningson 2002; Asai *et al.* 2002). Brandt & Henningson (2004) used varicose-like/sinuuous-like instability to identify the breakdown type in bypass transition subject to free stream turbulence. We refer to the patterns observed in figure 13 as inclined varicose-like/sinuuous-like instability in this work. It is worthy noting that here the secondary instability occurs on the negative streaks on each side, while in transition induced by a single roughness element, the instability is observed in the central region around the negative streak. Sinuuous instability mode is found in the near-wake of a thin roughness element, whereas varicose instability plays a key role in the larger element case (Loiseau *et al.* 2014).

To further investigate the breakdown type, the disturbance velocity is transferred to the Fourier space through Discrete Fourier Transform. Figure 14 provides the frequency spectra at $(x, y, z) = (78, 2.1, 7)$ for the narrow configuration and $(x, y, z) = (78, 2.1, 4.5)$ for the wide configuration, respectively. In figure 14(a) the peak for the narrow configuration is around $\omega = 0.18$ and broad-banded. The value of the second peak is close to the first one and the remaining peaks at higher frequencies are not clear. In figure 14(b), the peak of the spectrum occurs at $\omega = 0.22$ and the values for the remaining higher frequencies reduce gradually. A very similar observation is found in the experimental work of Puckert & Rist (2018) and Puckert & Rist (2019) where disturbance developed downstream of a roughness element is investigated. Puckert & Rist (2019) also reported a changeover of the Fourier spectra when increasing the Reynolds number. They observed varicose modes at subcritical Re where there are distinctive peaks in the Fourier spectra. At supercritical Re they found that the varicose and sinuuous modes coexist and are coupled by frequency lock-in.

The Fourier mode shape at $x = 78$ at frequencies marked in figure 14 are examined. Figure 15(a) and (b) presents two representative Fourier mode shapes in the narrow layout case between $\omega = 0.15$ and $\omega = 0.35$. In figure 15(a) the Fourier mode exhibits a clear asymmetric shape with respect to the inclined mean flow. On the other hand in figure 15(b) the mode shape is symmetric, similar to the varicose pattern (Asai *et al.* 2002). It therefore can be concluded that both the sinuuous-like and varicose-like types of

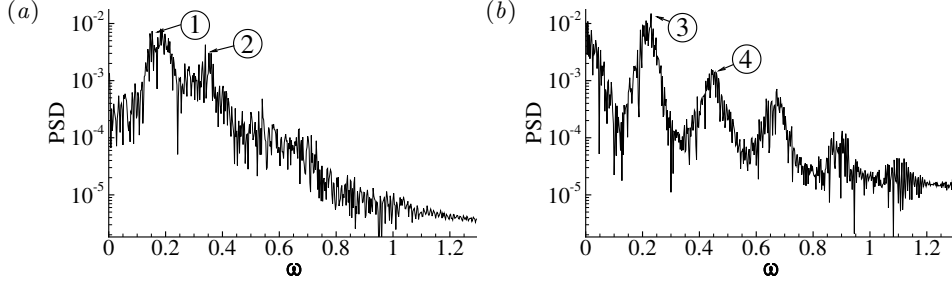


FIGURE 14. Fourier spectra for (a) $(L_x, L_z) = (90, 0.25)$ at $(x, y, z) = (78, 2.1, 7)$, which is marked by a solid green circle in figure 13(a), (b) $(L_x, L_z) = (90, 1)$ at $(x, y, z) = (78, 2.1, 4.5)$, which is marked by a solid green circle in figure 13(b).

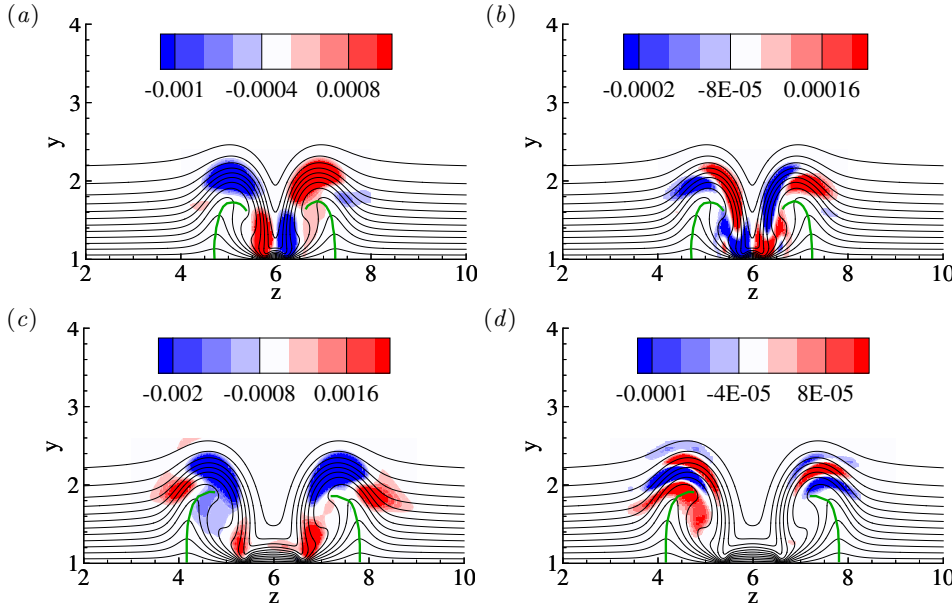


FIGURE 15. Contour of streamwise component of Fourier mode for narrow layout case at (a) $\omega = 0.18$, (b) $\omega = 0.29$, which correspond to ① and ② in figure 14(a), and wide layout case at (c) $\omega = 0.225$, (d) $\omega = 0.45$, which correspond to ③ and ④ in figure 14(b). Contour lines denote the streamwise mean velocity \bar{U} from 0.1 to 1.

instability exist in the transition downstream of plasma actuators with narrow spanwise distance. It is worth noting that most of the mode shapes that can be identified around the first frequency peak in figure 14(a) is asymmetric while most around the second frequency peak is symmetric, similar with the observation by Puckert & Rist (2019). In the case where the sinuous and varicose mode coexist, they also found a sinuous pattern of Fourier modes at a low frequency and a varicose pattern at a high frequency. In the wide layout case shown in figure 15(c) and (d), Fourier modes are computed at the peak frequencies and the perturbation patterns are similar as that in figure 13(b), confirming the inclined varicose-like instability for the wide configuration.

4.5. Tilting of disturbance

In this section, the third stage in figure 6 starting from $x = 85$ is discussed in detail. Figure 16 shows isosurfaces of the streamwise perturbation u'' in stage 3 for the narrow and

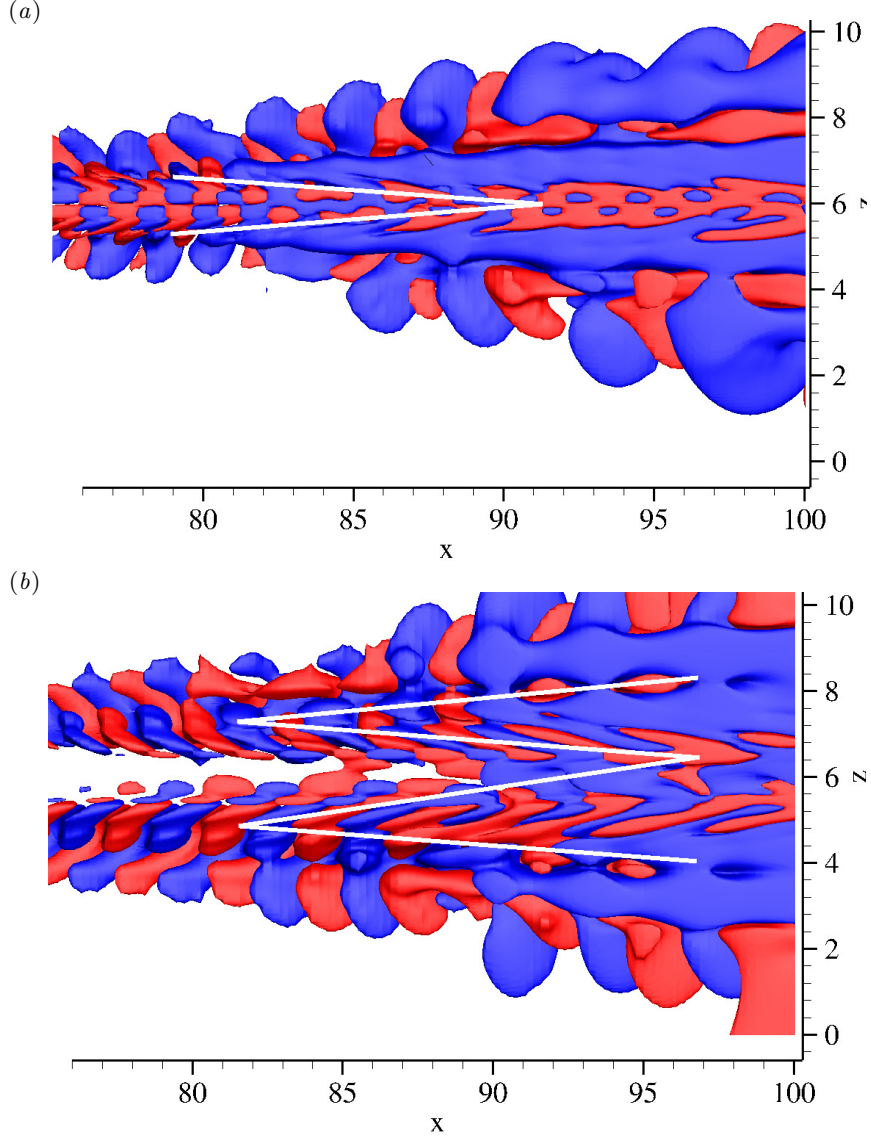


FIGURE 16. Isosurfaces of $u'' = 0.005$ (red) and $u'' = -0.005$ (blue) for (a) $(L_x, L_z) = (90, 0.25)$ and (b) $(L_x, L_z) = (90, 1)$. Note here positive wall-normal direction points into the paper. Solid white lines are drawn along the disturbance inclination and shows a ‘V’ and ‘W’ shapes in (a) and (b), respectively.

wide layouts, respectively. The velocity perturbation is further tilted along the direction of shear in the region between $x = 80$ to $x = 90$ downstream of the instability region where the structures are almost periodic in the streamwise direction. In figure 16(a), the disturbance is inclined towards the centre in the streamwise direction and displays a ‘V’ shape. In figure 16(b), the disturbance near the centre is tilted downstream, while those on the side are tilted upstream, resulting in a ‘W’ shape.

To explain the different patterns of inclination, we examine the mean spanwise shear in a $y - z$ plane at $x = 85$ in figure 17. In both layouts, regions of positive and negative spanwise shear are seen on the flanks of the negative streaks. Since the negative streaks

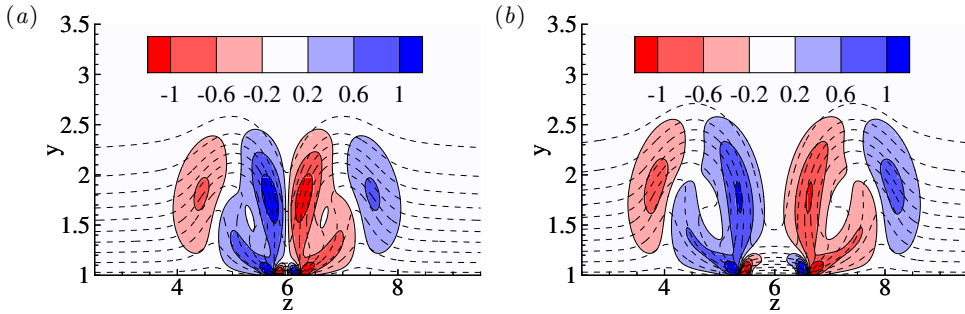


FIGURE 17. Contour of mean spanwise shear $d\bar{U}/dz$ at $x = 85$ for (a) $(L_x, L_z) = (90, 0.25)$ and (b) $(L_x, L_z) = (90, 1)$. Dashed contour lines denote the streamwise mean velocity \bar{U} from 0.1 to 1.

are inclined towards the centre, the mean shear on the side closer to the centre is stronger than that on the other side. In the narrow layout, the streaks are closer and the resulting mean spanwise shear and its gradient in the spanwise direction are stronger than those in the wide layout.

The effect of L_z on the disturbance is schematically represented in figure 18. The distribution of mean spanwise shear along the spanwise direction is plotted qualitatively by dashed lines. For extremely small values of L_z , the negative streaks appear close to each other and their width is significantly larger than that of the positive streak. The dashed line in the centre becomes almost vertical representing a sharp mean spanwise shear gradient at the centre. The spanwise shear in the centre is much stronger while those on the side becomes so small that they do not affect the disturbance and can be negligible. The disturbance is tilted forward by the mean shear in the centre, leading to the ‘V’ shape as seen in figure 16(a). As L_z increases, negative streaks become farther away from each other and the positive streak appears wider, consequently the dashed line in the centre turns anti-clockwisely. The strength of mean shear in the centre is reduced, while those on the side becomes stronger enough to tilt the disturbance backwards, leaving a ‘W’ shape with the two sides shorter than those in the middle. As L_z further increases, the positive and negative streaks are of similar width with spanwise shear of similar strength. Now the disturbance has a standard ‘W’ shape as shown in figure 16(b).

5. Linear analysis

The observations in § 4 from DNS results indicate linear dynamics such as secondary instability. These can be studied by linear modal and non-modal analysis as will be presented in § 5.1 and § 5.2 below.

5.1. Secondary instability analysis

In this section, linear analysis tools are used to verify and further clarify the DNS observations. In the second stage of the transition process induced by plasma actuation, there is evidence that both the sinuous-like and varicose-like mode exist in the narrow configuration, while in the wide layout, only varicose-like instability is identified. Biglobal stability analysis are used here to illustrate the secondary instability mechanism in stage 2. As the flow develop to turbulence downstream, time-averaged mean flow \bar{U} is used as the base flow for all simulations. The algorithms used have been well documented (Schmid & Henningson 2001) and will not be elaborated.

The secondary instability is evaluated at a cross-flow plane extracted from various

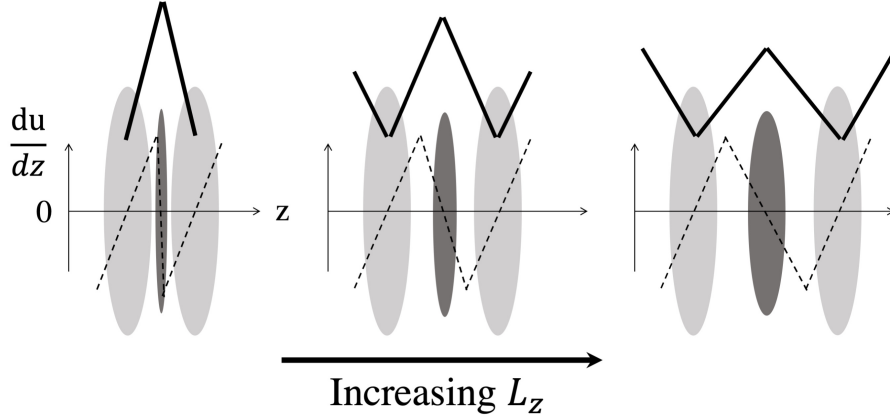


FIGURE 18. Schematic plot of streaks induced by plasma actuators. Dark and light grey colours denote positive and negative streaks, respectively; the dashed lines qualitatively represent the distribution of the mean spanwise shear along the spanwise direction; the solid lines indicate the transformation of the ‘V’ shape to the ‘W’ shape as L_z increases.

downstream locations in the region from $x = 35$ to $x = 80$ corresponding to stage 1 and 2 as identified in § 4.2. At each streamwise location, the streamwise wavenumber is varied from $\alpha = 0$ to $\alpha = 5$, corresponding to streamwise wavelength infinity and 1.25, respectively. The growth rates of the associated most unstable modes for each pair of (x, α) are obtained as plotted in figure 19. For both layouts, the onset of instability of the temporal modes appears at $x \approx 35$, at which the streak amplitude A reaches around 34% of the free stream velocity as shown in figure 10.

The contour plot of growth rate for the narrow configuration in figure 19(a) have two peaks. The larger peak is located at $x = 45$ and $\alpha = 1.8$ while the sub peak appears at $x = 55$ and $\alpha = 3$. These two peaks correspond to the sinuous and varicose modes and will be illustrated later. Moreover, the temporal frequency of these two peaks are 0.18 and 0.27, respectively, which are around ① and ② in figure 14(a), corresponding to the sinuous and varicose modes, respectively. In the wide configuration in figure 19(b), the peak of growth rates occurs at $x = 50$ and $\alpha = 2.4$. Similar as the narrow layout case, the temporal frequency of the most unstable mode is 0.23, which is in agreement with the peak frequency in figure 14(b). In both cases, the base (mean) flow becomes less unstable at larger x even though the streak amplitude continues to increase and reaches a peak at $x = 80$ in figure 10. This is associated with the change in the base (mean) flow. Figure 20 presents the mean spanwise shear of the base flow for the wide layout case as an example at four streamwise positions, which include one upstream of the peak, one at the peak and two downstream of the peak. As x increases, the base streak grows in size. However the change in the mean flow shape is different and leads to non-monotonically variation of the mean spanwise shear. In order to compare the mean shear clearly, three positive and negative levels are shown in Figure 20. From $x = 35$ to $x = 50$, the relative distribution of contour levels is almost the same and only the size of the region is expanding. The increase of mean shear leads to the increase of the growth rate from $x = 35$ to $x = 50$ in figure 19(b). From $x = 50$ onwards, although the overall region continues to expand as a result of the streak growth, the region of the highest contour level becomes smaller and even disappears at $x = 70$. Therefore the strength of the mean spanwise shear is the largest at $x = 50$, at which the mean flow shows the largest growth rate of secondary

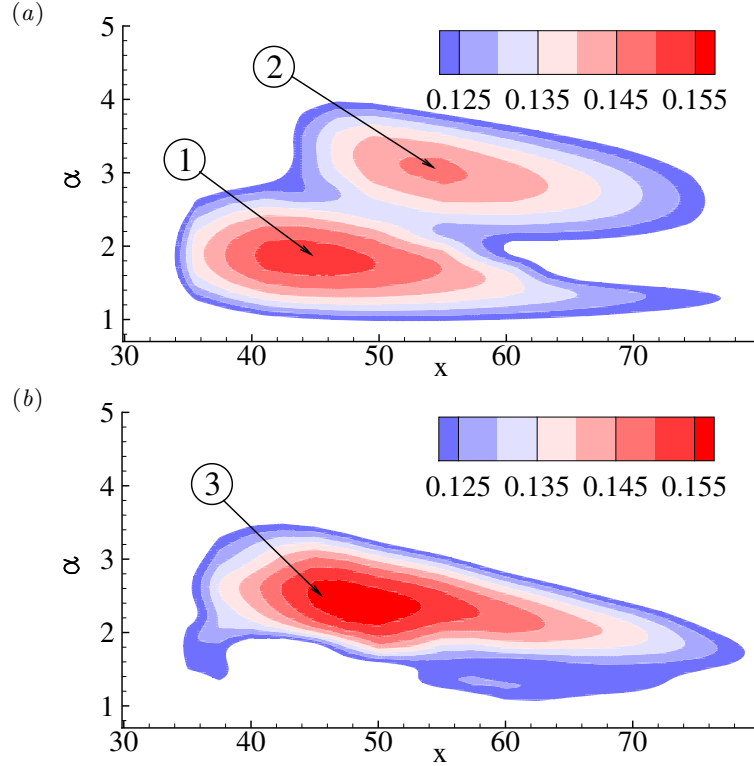


FIGURE 19. The secondary instability growth rate in $\alpha - x$ plane for (a) $(L_x, L_z) = (90, 0.25)$ and (b) $(L_x, L_z) = (90, 1)$.

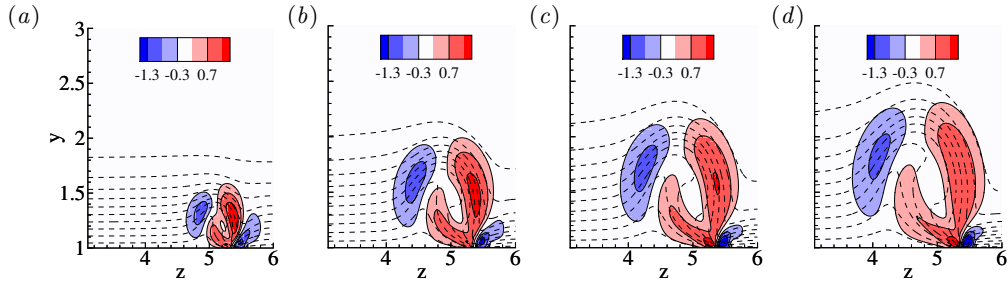


FIGURE 20. Contour of mean spanwise shear $d\bar{U}/dz$ for $(L_x, L_z) = (90, 1)$ at (a) $x = 35$, (b) $x = 50$, (c) $x = 60$ and (d) $x = 70$. Dashed contour lines denote the streamwise mean velocity \bar{U} from 0.1 to 1. Only half of the domain in spanwise direction is presented.

instability. Similar observations are made in the narrow layout case, i.e., $d\bar{U}/dz$ at the peak location $x = 45$ is the strongest, and is therefore not presented.

A representative eigenmode of the secondary instability near the peaks in the narrow and wide layouts are illustrated in figure 21, along with line contours of the streaky mean profile \bar{U} . For the narrow layout, the mode shape at the lower peak is asymmetric with respect to the negative streak and the one at the higher peak is symmetric, while for the wide layout, the secondary instability is symmetric. These confirm both types of instability exist in the narrow layout case while in the wide layout case there are only varicose-like modes.

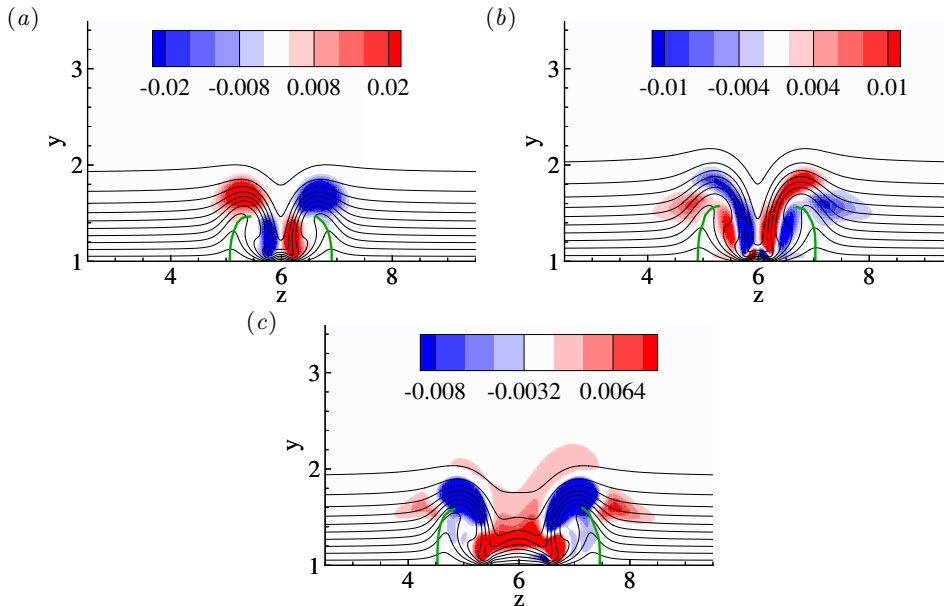


FIGURE 21. Secondary instability modes at (a) $x = 45$, $\alpha = 1.8$, corresponding to ① in figure 19(a); (b) $x = 55$, $\alpha = 3$, corresponding to ② in figure 19(b); (c) $x = 45$, $\alpha = 2.3$, corresponding to ③ in figure 19(b). Solid contour lines denote the streamwise mean velocity \bar{U} from 0.1 to 1.

5.2. Transient growth analysis

As mentioned previously, plasma actuators are analogous to roughness elements. It has been found that transient growth plays a significant role in roughness induced transition (White 2002; White *et al.* 2005; Downs *et al.* 2008). In this section, linear optimal transient growth analysis are performed to further investigate stage 3 from the DNS results in § 4.5. Similar as before, time-averaged mean flow \bar{U} is adopted as the base flow. Initial conditions that result in the largest transient energy growth G over a time horizon T is obtained,

$$G = \frac{E(T)}{E(0)}, \quad (5.1)$$

where E denotes the kinetic energy of the perturbation integrated over the computational domain Ω . The numerical solver used for the transient growth analysis involves solving the linearised Navier-Stokes equation and its adjoint, and has been verified in previous works (Barkley *et al.* 2008; Mao & Hussain 2017).

The variation of the maximum growth G with respect to T at different L_x and L_z are presented in figure 22. In figure 22(a), before reaching the peak G increases with T at similar rate for all cases. Moreover, larger L_x results in higher peak value of G because longer actuators lead to larger streak amplitude as shown in figure 8, in agreement with the findings in Cherubini *et al.* (2013) where transient growth analysis of flow past a roughness element was performed. The effect of L_z on G is similar as seen in figure 22(b). G for $(L_x, L_z) = (90, 0.1)$, which leads to only streaks without breakdown, is significantly smaller than those with larger L_z that results in turbulence.

The streamwise component of the initial condition that leads to the largest transient energy growth for the narrow and wide layout cases is presented in figure 23(a) and (b), respectively. In figure 23(a), the initial streamwise velocity neither resembles the optimal response for the varicose nor the sinuous perturbations found in literature as we have

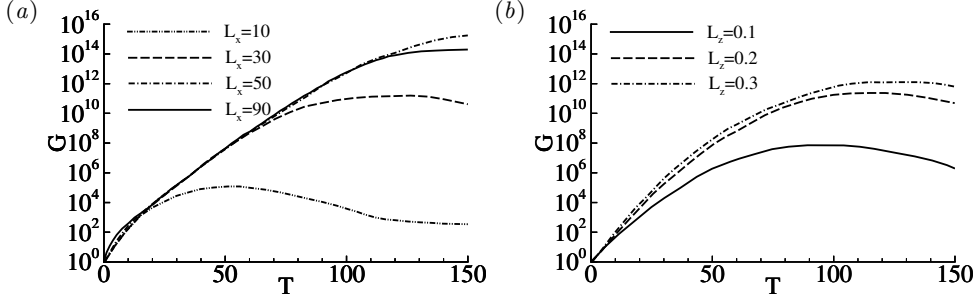


FIGURE 22. Maximum transient energy growth G versus T for (a) $L_z = 0.25$ and various values of L_x , (b) $L_x = 90$ and various values of L_z .

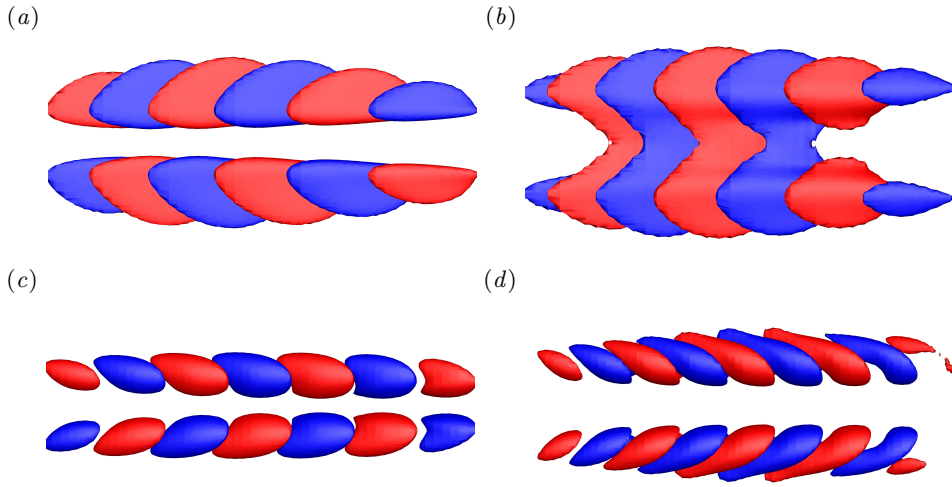


FIGURE 23. Isosurfaces of streamwise velocity of the initial conditions yielding the maximum energy growth (a,b) and their optimal response at $t = 90$ (c,d). (a,c) present the narrow layout case with $(L_x, L_z) = (90, 0.25)$ while (b) and (d) present the wide layout case with $(L_x, L_z) = (90, 1)$. The plots show the $x - z$ plane view. The isosurfaces represent areas where the value equals 0.2 of the maxima/minima.

seen both type of instability modes exist. In figure 23(b), the streamwise component on each side, concentrated in the region of strong wall-normal shear on the top of the streak, resembles the optimal initial streamwise velocity obtained for the varicose perturbation in Høpfner *et al.* (2005). This is another proof of the varicose-like type instabilities on the negative streaks in the wide layout. The velocity component in the narrow layout has a similar pattern as that in the wide layout, but is slightly tilted in the streamwise direction. Moreover, the streamwise velocity is asymmetric with respect to the centre in the narrow configuration and symmetric in the wide configuration, which is in agreement with the observations from DNS.

The optimal responses at $t = 90$ for the initial conditions in figure 23(a) and (b) are illustrated in figure 23(c) and (d). In both layouts the streamwise velocity component is the most amplified, which is also reported in previous work (Høpfner *et al.* 2005; Cherubini *et al.* 2013).

Figure 24 presents the same flow as in figure 23, but in the $x - y$ plane. In both cases, the streamwise components are initially backward-leaning against the shear. In figure

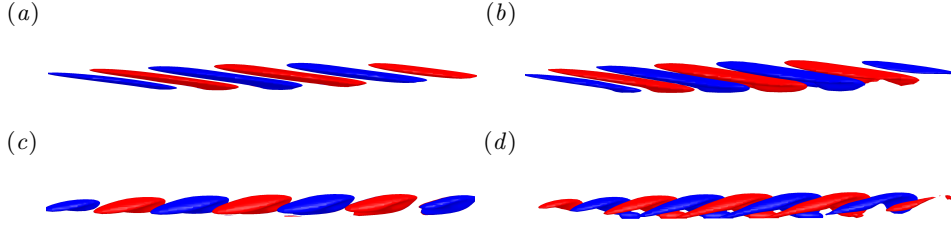


FIGURE 24. Isosurfaces of streamwise velocity of the initial conditions yielding the maximum energy growth (*a,b*) and their optimal response at $t = 90$ (*c,d*). (*a,c*) present the narrow layout case with $(L_x, L_z) = (90, 0.25)$ while (*b*) and (*d*) present the wide layout case with $(L_x, L_z) = (90, 1)$. The plots show the $x - y$ plane view. The isosurfaces represent areas where the value equals 0.2 of the maxima/minima.

24(c) and (d), the structures are tilted to be forward-leaning by the shear, suggesting the Orr mechanism in which perturbations gain transient energy growth when they are tilted from backward-leaning to normal and then decay when tilted to be forward-leaning. However, inspecting the history of flow development (not shown here), we observe that the forward-leaning structures only appear at $t < 10$. In figure 22, the growth lasts to $t \sim 100$, indicating that the Orr mechanism only contributes to the energy growth initially and the lift-up effect has a significant role in the energy growth in later time. Similar observations were reported by Hack & Moin (2017) who found that in non-parallel flow the energy growth of the most highly amplified perturbations is attributed to the combined action of the lift-up and Orr mechanism.

The isosurfaces in figure 23 and 24 represent values equal 0.2 of the maxima/minima and the flow structures are inclined in the streamwise direction due to the mean spanwise shear caused by the positive streak at the centre. In order to link the transient growth mode with previous DNS results, figure 25 displays the optimal response of streamwise velocity, similar as that in figure 23(c) and (d) but with the isosurfaces representing a much smaller value that corresponds to 0.022 of the maxima/minima. The plots are presented with positive wall-normal direction points into the paper. The ‘V’ shape in the narrow layout and ‘W’ shape in the wide layout observed in figure 16 can be clearly seen here, which support the findings in the DNS. Another observation that supports previous ones is that in figure 25(a) the velocity component starts to appear around the centre before expanding in the spanwise direction, while in the wide layout case in figure 25(b), the perturbations first appear on each side simultaneously and expand on their own, before merging together and then the Orr mechanism becomes dominant.

6. Conclusion

The response of a boundary layer flow over a flat plate to the actuation of a pair of DBD plasma actuators mounted on the plate is investigated numerically. A 4-species plasma-fluid model is used to model the EHD body force generated by the plasma actuators. A two-dimensional steady plasma force distribution is computed from a plasma solver and used to drive the transition in the three-dimensional boundary layer.

The body force generated by the plasma actuators results in a pair of counter-rotating streamwise vortices that lead to the formation of a high-speed streak in the centre and two low-speed streaks on either side. Both the streamwise length of actuators (L_x) and spanwise distance between the actuators (L_z) affect the flow development significantly. For small values of L_x , the streaks initially grow and start to decay immediately beyond

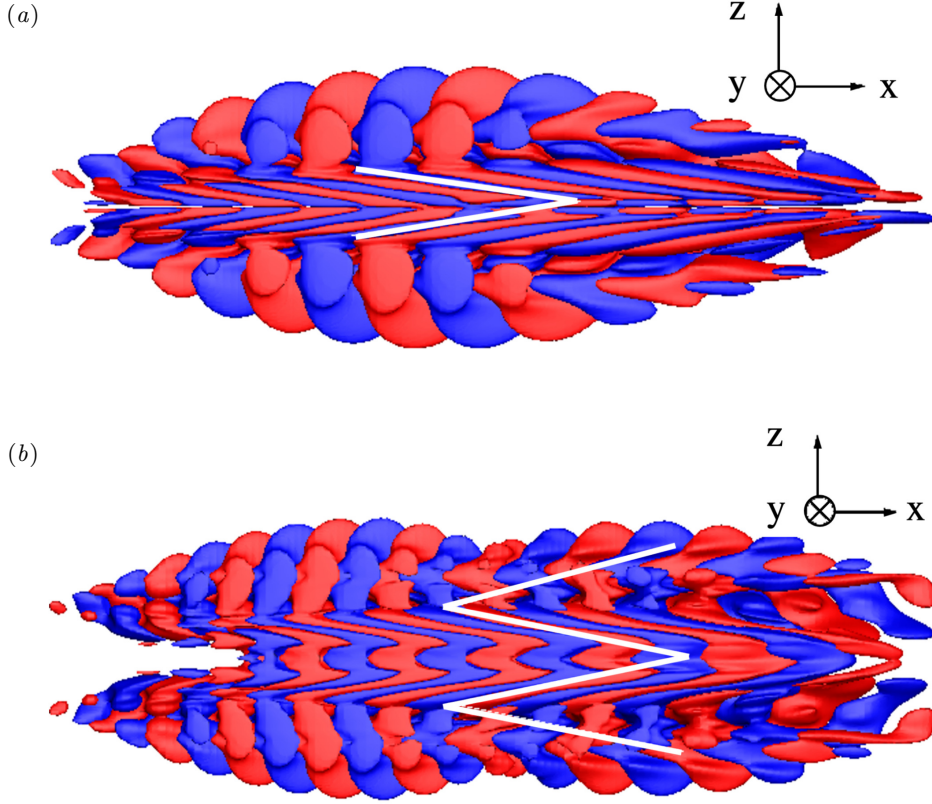


FIGURE 25. Isosurfaces of streamwise velocity of the final condition yielding maximum energy growth at $T = 120$ for (a) $(L_x, L_z) = (90, 0.25)$ and (b) $(L_x, L_z) = (90, 1)$. Both plots show in the $x - z$ plane with positive wall-normal direction pointing into the paper. The isosurfaces represent areas where the value equals 0.022 of the maxima/minima.

the actuator region. Larger L_x results in larger streak amplitude and bypass transition through a turbulent wedge. On the other hand, L_z determines the peak value of streak amplitude. For L_z below a certain value, the peak streak amplitude does not exceed the critical value and is maintained over the plasma region. In cases with larger L_z , bypass transition occurs at a similar location.

The bypass transition downstream of the plasma actuators can be divided into four stages: generation of streaks, secondary instability, tilting of perturbations and turbulent wedge. The second and third stage is investigated in detail through two cases: a narrow layout and a wide layout. In the former case, the positive and negative streaks are close in the spanwise direction, resulting in strong mean spanwise shear. This leads to secondary instability with an asymmetric pattern first appears on the high-speed streak in the centre. The low-speed streaks lose stability afterwards with evidence of both inclined sinuous-like and varicose-like modes. The perturbations remain asymmetric with respect to the centre. In the following tilting stage, the mean shear at the centre dominates and the perturbations appear in a 'V' pattern. In the latter case, the low-speed streak on each side experiences inclined varicose-like secondary instability simultaneously and therefore the perturbations have a symmetric pattern with respect to the centre. In the

third stage the perturbations expand in the spanwise direction via shear, which results in a ‘W’ pattern.

Global stability analysis are performed using the mean flow from DNS as the base profile to further examine the secondary instabilities. In the narrow configuration, two peaks of the growth rate on the streamwise location VS streamwise wavenumber plane are observed, corresponding to an inclined sinuous-like instability and a varicose-like one, while in the wide layout the mode shape at the peak of the growth rate is inclined varicose-like. The optimal initial condition from transient growth analysis is symmetric with respect to the centre for the wide configuration and asymmetric for the narrow configuration. The ‘V’ and ‘W’ pattern due to the shear is also observed in the flow response for the narrow and wide layout, respectively. In summary, the findings from DNS are confirmed by these linear analysis which further reveal the mechanism of the perturbation developments.

Acknowledgments

This work was supported by the Marie Skłodowska-Curie Research and Innovation Staff Exchanges programme [Grant No. 777717].

REFERENCES

- ANDERSSON, P., BERGGREN, M. & HENNINGSON, D. S. 1999 Optimal disturbances and bypass transition in boundary layers. *Phys. Fluids* **11**, 134–150.
- ANDERSSON, P., BRANDT, L., BOTTARO, A. & HENNINGSON, D. S. 2001 On the breakdown of boundary layer streaks. *J. Fluid Mech.* **428**, 29–60.
- ASAI, M., MINAGAWA, M. & NISHIOKA, M. 2002 The instability and breakdown of a near-wall low-speed streak. *J. Fluid Mech.* **455**, 289–314.
- BADE, K. M., HANSON, R. E., BELSON, B. A., NAGUIB, A. M., LAVOIE, P. & ROWLEY, C. W. 2016 Reactive control of isolated unsteady streaks in a laminar boundary layer. *J. Fluid Mech.* **795**, 808–846.
- BARKLEY, D., BLACKBURN, H. M. & SHERWIN, S. J. 2008 Direct optimal growth analysis for timesteppers. *Intl J. Numer. Meth. Fluids* **57**, 1435–1458.
- BIANCOFIORE, L., BRANDT, L. & ZAKI, T.A. 2017 Streak instability in viscoelastic couette flow. *Phys. Rev. Fluids* **2**, 1–20.
- BOEUF, J. P., LAGMICH, Y., UNFER, TH. & PITCHFORD, L. C. 2007 Electrohydrodynamic force in dielectric barrier discharge plasma actuators. *J. Phys. D: Appl. Phys* **40**, 652–662.
- BRANDT, L. & HENNINGSON, D. S. 2002 Transition of streamwise streaks in zero-pressure-gradient boundary layers. *J. Fluid Mech.* **472**, 229–261.
- BRANDT, L. & HENNINGSON, P.S. SCHLATTER D. S. 2004 Transition in boundary layers subject to free-stream turbulence. *J. Fluid Mech.* **517**, 167–198.
- BUCCI, M. A., PUCKERT, D. K., ANDRIANO, C., LOISEAU, J. CH., CHERUBINI, S., ROBINET, J. CH. & RIST, U. 2018 Roughness-induced transition by quasi-resonance of a varicose global mode. *J. Fluid Mech.* **836**, 167–191.
- BUTLER, K. M. & FARRELL, B. F. 1992 Three-dimensional optimal perturbations in viscous shear flow. *Phys. Fluids A* **4(8)**, 1637–1650.
- CHERUBINI, S., TULLIO, M. D. DE, PALMA, P. DE & PASCAZIO, G. 2013 Transient growth in the flow past a three-dimensional smooth roughness element. *J. Fluid Mech.* **724**, 624–670.
- CHOI, K. S., JUKES, T. N. & WHALLEY, R. D. 2011 Turbulent boundary-layer control with plasma actuators. *Phil. Trans. R. Soc. A* **369**, 1443–1458.
- CHOI, K. S. & KIM, J. H. 2018 Plasma virtual roughness elements for cross-flow instability control. *Exp. Fluids* **59**, 159.
- COSSU, C. & BRANDT, L. 2002 Stabilization of tollmien-schlichting waves by finite amplitude optimal streaks in the blasius boundary layer. *Phys. Fluids* **14**, L57.
- VON DEYN, L. H., FOROOGHI, P., FROHNAPFEL, B., SCHLATTER, P., HANIFI, A. & HEN-

- NINGSON, D. S. 2020 Direct numerical simulations of bypass transition over distributed roughness. *AIAA J.* **58**(2), 702–711.
- DOWNS, R. S., WHITE, E. B. & DENISSEN, N. A. 2008 Transient growth and transition induced by random distributed roughness. *AIAA J.* **46**(2), 451–462.
- DUCHMANN, A., GRUNDMANN, S. & TROPEA, C. 2014 Delay of natural transition with dielectric barrier discharges. *Exp. Fluids* **54**, 1–12.
- DUFOUR, G. & ROGIER, F. 2015 Numerical modeling of dielectric barrier discharge based plasma actuators for flow control: the COPAIER/CEDRE example. *AerospaceLab* **10**, 12726.
- FENG, L., JUKES, T., CHOI, K. S. & WANG, J. 2012 Flow control over a naca 0012 airfoil using dielectric-barrier-discharge plasma actuator with a gurney flap. *Exp. Fluids* **52**, 1533–1546.
- FRANSSON, J. H. M., MATSUBARA, M. & ALFREDSSON, P. H. 2005 Transition induced by free-stream turbulence. *J. Fluid Mech.* **527**, 1–25.
- GASTER, M., GROSCH, C. E. & JACKSON, T. L. 1994 The velocity field created by a shallow bump in a boundary layer. *Phys. Fluids* **6**(9), 3079–3085.
- GIORGI, M. G. DE, FICARELLA, A., MARRA, F. & PESCHINI, E. 2017 Micro dbd plasma actuators for flow separation control on a low pressure turbine at high altitude flight operating conditions of aircraft engines. *Appl. Thermal Eng.* **114**, 511–522.
- GOLDSTEIN, D. B., CHU, J. & BROWN, G. L. 2017 Lateral spreading mechanism of a turbulent spot and a turbulent wedge. *Flow Turbulence Combust* **98**, 21–35.
- GOUDER, K. A., NAGUIB, A. M., LAVOIE, P. L. & MORRISON, J. F. 2017 Control of boundary layer streaks induced by freestream turbulence using plasma actuators. *10th Intl. Symp. on Turbulence and Shear Flow Phenomena 2017*.
- GREENBELT, D., SCHNEIDER, T. & SCHULE, C. Y. 2012 Mechanism of flow separation control using plasma actuation. *Phys. Fluids* **24**, 077102.
- GRUNDMANN, S. & TROPEA, C. 2008 Active cancellation of artificially induced tollmien-schlichting waves using plasma actuators. *Exp. Fluids* **44**, 795–806.
- HACK, M. & ZAKI, T. A. 2014 Streak instabilities in boundary layers beneath free-stream turbulence. *J. Fluid Mech.* **741**, 280–315.
- HACK, M. J. P. & MOIN, P. 2017 Algebraic disturbance growth by interaction of orr and lift-up mechanisms. *J. Fluid Mech.* **829**, 112–126.
- HAGELAAR, G. J. M. & PITCHFORD, L. C. 2005 Solving the boltzmann equation to obtain electron transport coefficients and rate coefficients for fluid modes. *Plasma Sources Science and Technology* **14**(4).
- HÖPFFNER, J., BRANDT, L. & HENNINGSON, D. S. 2005 Transient growth on boundary layer streaks. *J. Fluid Mech.* **537**, 91–100.
- HUANG, W., XIAO, D., REN, J., WANG, Z., XI, G. & MAO, X. 2021 Bypass transition in flow over a vibrating flat plate. *J. Fluid Mech.* **909**.
- HUNT, J. & DURBIN, P. A. 1999 Perturbed vortical layers and shear sheltering. *Fluid Dyn. Res.* **24**, 375.
- JACOBS, R. G. & DURBIN, P. A. 2001 Simulations of bypass transition. *J. Fluid Mech.* **428**, 185–212.
- JUKES, T. N. & CHOI, K. S. 2012 Dielectric-barrier-discharge vortex generators: characterisation and optimisation for flow separation control. *Exp. Fluids* **52**(2), 329–345.
- JUKES, T. N. & CHOI, K. S. 2013 On the formation of streamwise vortices by plasma vortex generators. *J. Fluid Mech.* **733**, 370–393.
- JUKES, T. N., CHOI, K. S., SEGAWA, T. & YOSHIDA, H. 2008 Jet flow induced by a surface plasma actuator. *Proc. Inst. Mech. Engrs I* **222**, 347–356.
- KENDALL, J. M. 1985 Experiments on boundary-layer receptivity to freestream turbulence. *AIAA Paper* pp. 85–1695.
- KOURTZANIDIS, K., DUFOUR, G. & ROGIER, F. 2020a Explaining the electrohydrodynamic force and ionic wind spatiotemporal distribution in surface ac dielectric barrier discharge actuators.
- KOURTZANIDIS, K., DUFOUR, G. & ROGIER, F. 2020b Self-consistent modeling of a surface ac dielectric barrier discharge actuator: in-depth analysis of positive and negative phases. *J. Phys. D: Appl. Phys* **54**(4), 045203.
- LANDAHL, M. T. 1975 Wave breakdown and turbulence. *SIAM J. Appl. Maths* **28**, 735–756.

- LANDAHL, M. T. 1980 A note on an algebraic instability of inviscid parallel shear flows. *J. Fluid Mech.* **98**, 243–251.
- LAVOIE, R. E. HANSON P., NAGUIB, A. M. & MORRISON, J. F. 2010 Transient growth instability cancelation by a plasma actuator array. *Exp. Fluids* **49**, 1339–48.
- LITTLE, J., NISHINARA, M., ADAMOVICH, I. & SAMIMY, M. 2010 High-lift airfoil trailing edge separation control using a single dielectric barrier discharge plasma actuator. *Exp. Fluids* **48**, 521–537.
- LOISEAU, J. C., ROBINET, J. C., CHERUBINI, S. & LERICHE, E. 2014 Investigation of the roughness induced transition: global stability analyses and direct numerical simulations. *J. Fluid Mech.* **760**, 175–211.
- MAHFOZE, O. & LAIZET, S. 2017 Skin-friction drag reduction in a channel flow with streamwise-aligned plasma actuators. *Int. J. Heat Fluid Flow* **66**, 83–94.
- MAO, X. 2015 Effects of base flow modifications on noise amplifications: flow past a backward-facing step. *J. Fluid Mech.* **771**, 229–263.
- MAO, X. & HUSSAIN, F. 2017 Optimal transient growth on a vortex ring and its transition via cascade of ringlets. *J. Fluid Mech.* **832**, 269–286.
- MAO, X., ZAKI, T. A., BLACKBURN, H. M. & SHERWIN, S. J. 2017 Transition induced by linear and nonlinear perturbation growth in flow past a compressor blade. *J. Fluid Mech.* **820**, 604–632.
- MATSUBARA, M. & ALFREDSSON, P. H. 2001 Disturbance growth in boundary layer subjected to free-stream turbulence. *J. Fluid Mech.* **430**, 149–168.
- MERTZ, B. E. & CORKE, T. C. 2011 Single-dielectric barrier discharge plasma actuator modelling and validation. *J. Fluid Mech.* **669**, 557–583.
- MONOKROUSOS, A., ÅKERVIK, E., BRANDT, L. & HENNINGSON, D. S. 2010 Global three-dimensional optimal disturbances in the blasius boundary-layer flow using time-steppers. *J. Fluid Mech.* **650**, 181–214.
- MOREAU, E. 2007 Airflow control by non-thermal plasma actuators. *J. Phys. D: Appl. Phys* **40(3)**, 605–636.
- NISHIDA, H., NONOMURA, T. & ABE, T. 2014 Three-dimensional simulations of discharge plasma evolution on a dielectric barrier discharge plasma actuator. *J. Appl. Phys.* **115(13)**.
- PHELPS, A. V. 2012 Phelps database. *LXCat* .
- PITCHFORD, L. C. & BOEUF, J. P. 2012 Siglo database, lxcat. *LXCat* .
- PUCKERT, D. K. & RIST, U. 2018 Global instability in a laminar boundary layer perturbed by an isolated roughness element. *Exp. Fluids* **59**, 48.
- PUCKERT, D. K. & RIST, U. 2019 Experimental observation of frequency lock-in of roughness-induced instabilities in a laminar boundary layer. *J. Fluid Mech.* **870**, 680–697.
- RIHERD, M. & ROY, S. 2013 Damping tollmien-schlichting waves in a boundary layer using plasma actuators. *J. Phys. D: Appl. Phys* **45**, 485203.
- RIHERD, M. & ROY, S. 2014 Stabilization of boundary layer streaks by plasma actuators. *J. Phys. D: Appl. Phys* **47**, 125203.
- SAIKISHAN, S., GOLDSTEIN, D. B. & BROWN, G. L. 2019 Roughness induced transition: A vorticity point of view. *Phys. Fluids* **31(2)**, 024101.
- SCHATZMAN, D. & THOMAS, F. 2010 Turbulent boundary-layer separation control with single dielectric barrier discharge plasma actuators. *AIAA J.* **48(8)**, 1620–1634.
- SCHMID, P. J. & HENNINGSON, D. S. 2001 Stability and transition in shear flows .
- SCHUBAUER, G. B. & KLEBANOFF, P. S. 1955 Contributions on the mechanics of boundary-layer transition. *NACA N-3489* .
- SHYY, W., JAYARAMAN, B. & ANDERSSON, A. 2002 Single-dielectric barrier discharge plasma actuator modelling and validation. *J. Fluid Mech.* **92(11)**, 6434–6443.
- SUZEN, Y., HUANG, P., JACOB, J. & ASHPIS, D. 2005 Numerical simulations of plasma based flow control applications. *AIAA Paper* **2005-4633**.
- SWEARINGEN, J. D. & BLACKWELDER, R. F. 1987 The growth and breakdown of streamwise vortices in the presence of a wall. *J. Fluid Mech.* **182**, 255–290.
- TAYLOR, G. I. 1939 Some recent development in the study of turbulence. *Proceedings of the Fifth International Congress for Applied Mechanics* (ed. JP Den Hartog and H. Peters) **531**, 294–310.

- THOMAS, C. C., ENLOE, C. L. & WILKINSON, S. P. 2010 Dielectric barrier discharge plasma actuators for flow control. *Annu. Rev. Fluid Mech.* **42**, 505–29.
- TULLIO, N. DE, PAREDES, P., SANDHAM, N. D. & THEOFILIS, V. 2013 Lamina-turbulent transition induced by a discrete roughness element in a supersonic boundary layer. *J. Fluid Mech.* **735**, 613–646.
- VAUGHAN, N. & ZAKI, T. A. 2011 Stability of zero-pressure-gradient boundary layer distorted by unsteady klebanoff streaks. *J. Fluid Mech.* **681**, 116–153.
- WALKER, S. & SEGAWA, T. 2012 Mitigation of flow separation using dbd plasma actuators on airfoils: A tool for more efficient wind turbine operation. *Renewable Energy* **42**, 105–110.
- WANG, B., MAO, X. & ZAKI, T. A. 2019 Low-frequency selectivity in flat-plate boundary layer with elliptic leading edge. *J. Fluid Mech.* **866**, 239–262.
- WHALLEY, R. D. & CHOI, K. S. 2013 The starting vortex in quiescent air induced by dielectric-barrier-discharge plasma. *J. Fluid Mech.* **703**, 192–203.
- WHITE, E. B. 2002 Transient growth of stationary disturbances in a flat plate boundary layer. *Phys. Fluids* **14(12)**, 4429–4439.
- WHITE, E. B., RICE, J. M. & ERGIN, F. G. 2005 Receptivity of stationary transient disturbances to surface roughness. *Phys. Fluids* **17(6)**, 064109.
- WILKINSON, S. 2003 Oscillating plasma for turbulent boundary layer drag reduction. *41st AIAA Aerospace Sciences Meeting, AIAA Paper* pp. 2003–1023.
- ZAKI, T. A. & DURBIN, P. A. 2005 Mode interaction and the bypass route to transition. *J. Fluid Mech.* **531**, 85–111.
- ZHONG, S., CHONG, T. P. & HODSON, H. P. 2003 A comparison of spreading angles of turbulent wedges in velocity and thermal boundary layers. *J. Fluids Eng* **125(2)**, 267–274.